Acta Metallurgica Sinica (English Letters) (2021) 34:1695–1703
https://doi.org/10.1007/s40195-021-01232-2

Effects of MeV Fe Ions Irradiation on the Microstructure and Property of Nuclear Grade 304 Stainless Steel: Characterized by Positron Annihilation Spectroscopy, Transmission Electron Microscope and Nanoindentation

Honglin Yan[1,2] · Zhiming Zhang[1] · Jianqiu Wang[1] · Bright O. Okonkwo[1,2] · En-Hou Han[1]

Received: 9 November 2020 / Revised: 18 January 2021 / Accepted: 26 January 2021 / Published online: 14 May 2021
© The Chinese Society for Metals (CSM) and Springer-Verlag GmbH Germany, part of Springer Nature 2021

Abstract
Nuclear grade 304 stainless steel was irradiated by 3.5 MeV Fe ions, with fluxes of 3.05E+15 ions/cm^2 and 1.55E+16 ions/cm^2. Irradiation effects were studied by positron annihilation spectroscopy (PAS), transmission electron microscope (TEM) and nanoindentation techniques. PAS results showed that different types of defects were produced after irradiation and that there was significant variance in defects formed when the samples were subjected to different irradiation doses. TEM characterization showed that the irradiation-induced dislocation loops enlarged in average size, but decreased in number density at higher irradiation doses. Nanoindentation test showed obvious irradiation hardening phenomenon, which was in good agreement with the PAS and TEM results. Irradiation hardening effect increased with an increase in irradiation dose and saturation occurred with an increase in irradiation dose from 3.2 to 16 dpa. Further statistical analysis showed that barrier strength of the Frank loop depends on the loop size and density produced by the ion irradiation.

Keywords Stainless steel · Irradiation hardening · Positron annihilation · Nanoindentation

1 Introduction

Type 304 austenitic stainless steel is widely used to fabricate nuclear structures like core reactor components, due to its good mechanical properties and excellent corrosion resistance [1, 2]. The service life of an operational nuclear power plant (NPP) relies on the safety of nuclear power structural components, such as the 304 stainless steel. The harsh environment of a nuclear power plant, such as high temperature, aggressive solution environment and high doses of neutron radiation and fission fragments from the core, had made it vital for the study of these effects on the NPP structural components [3]. Irradiation is known to have significant influence on the performance of nuclear power materials [4, 5]. Some of the effects arising from irradiation are irradiation hardening and embrittlement, irradiation segregation, creep, swelling and brittleness [2, 6, 7]. These effects accelerate the failure process of the NPP materials. According to the literature [8–10], irradiation-assisted stress corrosion cracking (IASCC) has become the main failure mode of core reactor materials. Irradiation causes hardening of materials, thereby leading to the increased strength and the plasticity reduction, which are important reasons for IASCC. Andresen et al. [11] showed that the yield strength of a material could significantly affect the SCC behavior. Irradiation hardening modifies the stress state at the crack tip, reduces the fracture toughness of the material and invariably improves the IASCC sensitivity of the material.

For the irradiation study, the use of ion implantation to simulate neutron irradiation has the advantages of short experimental period, accurate artificial control of irradiation parameters and low cost. Was et al. [12] found that similar results to neutron irradiation could be obtained by heavy ion irradiation. In addition, the use of ion irradiation facilitates the

Available online at http://link.springer.com/journal/40195

✉ Zhiming Zhang
zmzhang@imr.ac.cn

1 Key Laboratory of Nuclear Materials and Safety Assessment, Institute of Metal Research, Chinese Academy of Sciences, Shenyang 110016, China

2 School of Materials Science and Engineering, University of Science and Technology of China, Shenyang 110016, China

study of the formation of point defects and the reaction process caused by irradiation [13]. Also, previous studies have verified that bombarding a metallic material with heavy ion beams can cause significant hardening on the surface of the material [14, 15]. However, unlike neutron or proton irradiation, the depth of incidence of heavy ions in solid materials is very shallow, only a few microns [16, 17]. Nevertheless, the nanoindentation technique can accurately give the mechanical properties of the material near the surface layer, which can be used to characterize the hardening of the material under heavy ion irradiation [18, 19]. It is important to clarify microstructural changes during the irradiation process and fully understand the relationship between mechanical properties and the microstructural evolution. To compensate for the shortage of the detection limit for radiation defects by using traditional transmission electron microscope, positron annihilation spectroscopy (PAS) could provide more detailed features beyond recognition ability of traditional TEM. PAS is a detection technique for analyzing ultra-fine defects in materials and can be used to analyze defects caused by heavy ion irradiation [20]. Combining the PAS with TEM, the root cause of the hardening effect and the visible defect features induced by heavy ion irradiation can be analyzed better.

In this study, 3.5 MeV Fe ion was used to irradiate domestic nuclear grade 304 stainless steel. PAS, TEM and nanoindentation techniques were used to characterize the microstructural changes and concurrent irradiation hardening of the material. The results gave further information on the effect of heavy ion irradiation on the microstructure and irradiation hardening of core reactor material.

2 Experimental

The material used in this study is nuclear grade 304 stainless steel with solution treatment. The solution temperature was kept at 1050 °C for 30 min. Chemical composition of the material is listed in Table 1. First, a piece of 10 mm × 10 mm × 1 mm was cut from the original material by wire electrical discharge machining (WEDM). Thereafter, the cut piece was ground with SiC sand paper up to 5000 grit and mechanically polished with diamond paste. Finally, all specimens were polished in silicon oxide suspension to further remove the hardened layer.

The experimental work was carried out at the 320 kV platform for multi-discipline research with highly charged ions at Institute of Modern Physics, Chinese Academy of Sciences. The specimen was irradiated at ambient temperature by 3.5 MeV Fe^{13+} ions with fluxes of 3.05E+15 ions/cm^2 and 1.55E+16 ions/cm^2. Silver conductive adhesive was used to maintain a good electrical conductivity and thermal conductivity. Vacancy production of 3.5 MeV Fe ions irradiation in 304SS was calculated by SRIM-2008 using Kinchin-Pease approximation [21, 22], as shown in Fig. 1. Displacement energy (E_d) of 25 eV was used for the material [23]. Hence, the damage profile can be obtained. Values at the damage peak were 3.2 dpa (displacement per atom, dpa) and 16 dpa, respectively.

Doppler broadening of PAS was conducted in Key Laboratory of Nuclear Analysis Techniques, Institute of High Energy Physics, Chinese Academy of Sciences. The ^{22}Na radioactive source was used as a positron source, and the positron energy incident on the sample was continuously adjusted. Incident positron energies E_p varies from 0.03 to 25.0 keV and a high purity-Ge detector with an energy resolution of 1.2–1.3 keV at 511 keV peak was used to record the annihilation γ energy spectra [24]. More than 500 thousand annihilation events with a count rate of 1000 cps in the 511 keV peak were collected in each Doppler broadening spectrum (DBS). The total peak energy collected from the gamma spectrum was in the range of 499.5–522.5 keV. The spectrum was characterized by the two-standard line-shape parameters S and W, as demonstrated in Fig. 2; S represents the fractional area of the central portion of the peak (ranging from 510.2 to 511.8 keV) reflecting primarily annihilation with lower-momentum (e.g., valence, conduction) electrons in the material, while W parameter is the fractional area of the extreme wings of the photo-peak (ranging from 513.6

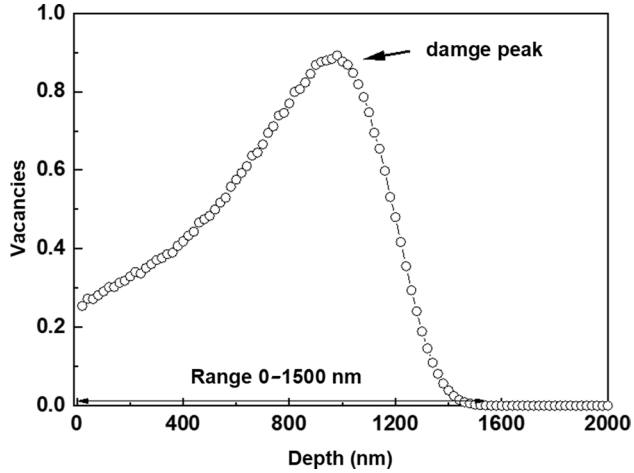

Fig. 1 Vacancy production by 3.5 MeV Fe ions in 304 SS. Recoil/damage calculations were made with Kinchin–Pease estimates

Table 1 Chemical composition of 304SS (wt%)

C	Cr	Ni	N	Mn	Si	S	P	Fe
0.053	18.45	8.30	0.057	1.59	0.47	0.004	0.022	Bal.

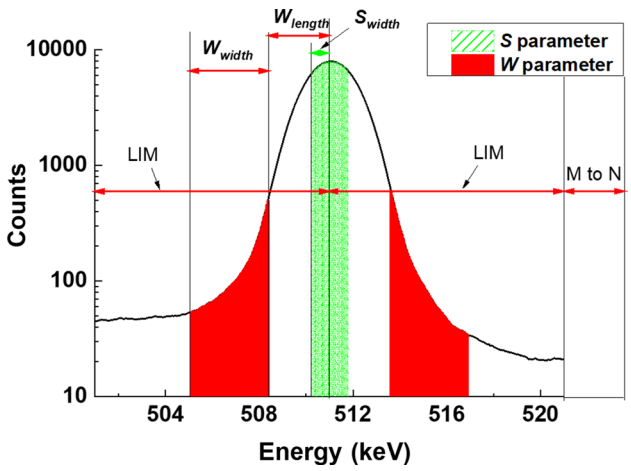

Fig. 2 Schematic diagram of *S* and *W* parameters in Doppler broadening of PAS. *S* represents the fractional area of the central portion of the peak, while *W* parameter is the fractional area of the extreme wings of the photo-peak

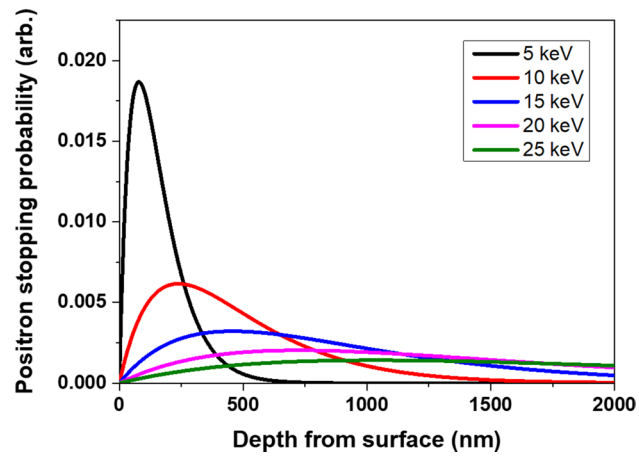

Fig. 3 Positron depth profiles with typical energies of 5, 10, 15, 20, 25 keV

to 516.9 keV and 505.1 to 508.4 keV) associated with annihilation with higher-momentum (e.g., core) electrons. *S* parameter and *W* parameter were calculated by the system software, with a relative accuracy of 0.001.

TEM foils were prepared using a Helios Nanolab 600i focused ion beam system (FIB). The irradiation-induced defects were characterized by using a JEM-2100F transmission electron microscope. Statistically, observation of the defects was performed at a distance of about one-micron depth away from the sample, i.e., the peak of the damage. It is known that the defects caused by the irradiation in austenitic stainless steel are mainly the interstitial Frank dislocation loops with a Burgers vector of $\boldsymbol{a}/3\langle 111\rangle$, distributed on the $\{111\}$ plane [25]. For each irradiated sample, more than four frames were used to determine the characteristics of these loops. Nanoindentation was performed with the Nano Indenter G200 (Agilent Corp.). A diamond Berkovich tip was used with continuous stiffness measurement (CSM) method. Samples were mounted onto aluminum stubs with hot wax, and indents were made in a direction normal to the sample surface. The strain rate and frequency were 0.05 s^{-1} and 45 Hz, respectively. Each specimen was subjected to 15 indentations with a spacing of 50 µm. Results were analyzed according to the method developed by Oliver and Pharr [26].

3 Results and Discussion

3.1 PAS

The positron depth profiles and the mean implantation depth were calculated based on the Makhovian equation [27]. Positron implantation distribution profile is given by:

$$P(z, E) = (m/z_0)(z/z_0)^{m-1} \exp\left[-(z/z_0)^m\right], \quad (1)$$

$$z_0(E) = z_{1/2}(E)(\ln 2)^{-1/m}, \quad (2)$$

where m is a material related constant with value of 2 and E is the energy of incident positron, and in this work, it varies from 0.03 to 25.0 keV. $z_{1/2}$ is the mean implantation depth of the positron in the material, which can be estimated by Eq. (3) [28]:

$$z_{1/2} = \frac{40}{\rho} E^{1.6}, \quad (3)$$

where ρ is density of the material in (g/cm^3) and E is the energy of the incident positron (in keV). The calculated profile is shown in Fig. 3.

The *S*-*E* curve is shown in Fig. 4. For non-irradiated sample, *S* parameter decreases rapidly with the increase in positron energy (i.e., the average incident depth) and tends to be stable after several hundred nanometers. This is because the vacancy defects in the unirradiated sample material are more evenly distributed, and therefore the probability of submerged positron coincides with their distribution inside the material. The high *S* parameter at low incident positron energies is due to positron diffusion to the surface and consequent production of ortho-positronium [29, 30]. For irradiated samples, the trends of *S*-*E* curves at the two irradiated doses are similar. With the increase in average positron incident depth, the *S* parameter increases rapidly and reaches a stable level after reaching the depth of several hundred nanometers. Within the range of 200 nm near the surface, the *S* parameter increases rapidly, indicating that the concentration of vacancy-type defects in the material increased rapidly. Beyond this range, the *S* parameter tends to be stable. The reason may come from two aspects: Firstly,

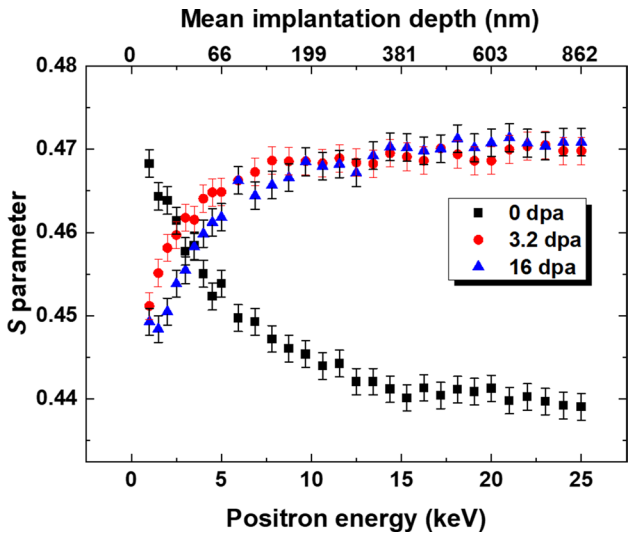

Fig. 4 *S* parameter versus positron energy (mean implantation depth) plots for the irradiated and unirradiated samples

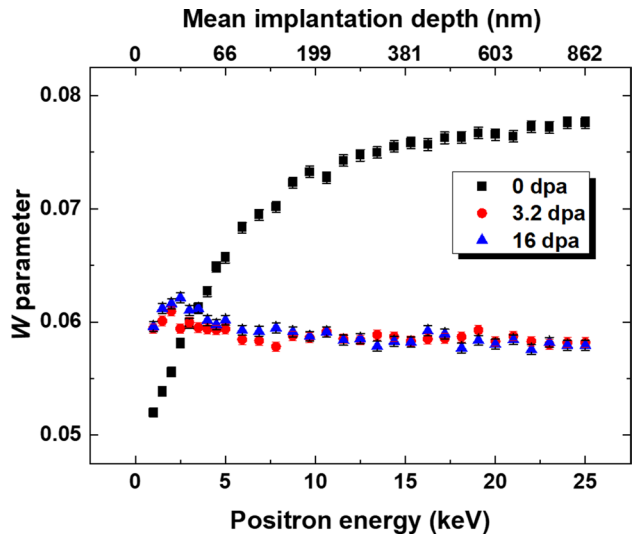

Fig. 5 *W* parameter versus positron energy (mean implantation depth) plots for the irradiated and unirradiated samples

the concentration of vacancy-type defects in the material has reached its saturation point at this dose. Secondly, it may due to the influence of matrix. With the positron energy increases, the average depth of incidence increases as well (Fig. 3), thereby detecting much of the information from the "substrate" (unirradiated region). Therefore, the *S* parameters tend towards being stable finally. Although the trends of *S*-*E* curves of irradiated samples at two different doses are similar, slight differences were also observed: in the range of 200 nm near the surface, the *S*-value of the low-dose irradiation sample was rather high, while beyond the 200-nm range, the *S*-value of the higher dose irradiated sample was slightly higher. This is because diffusion process along the short-circuits such as grain boundary was likely to be enhanced. The interstitials can efficiently diffuse from the ion deposition region into the near-surface region and therefore, which favor the recombination process [24]. Also, in addition to the recovery of the primary knock-on defects, under the irradiation with higher doses, the near surface of the material might be overheated, thereby resulting in thermal recovery of internal defects at elevated temperature [31]. In contrast, the highest vacancy defects were observed near the surface of the material at low doses. Therefore, it can be inferred that the number of dislocations produced by irradiation at low doses may be higher. In general, the *W* parameter and the *S* parameter should show opposite trends of variation. For the unirradiated sample as shown in Fig. 5, the *W* parameter increases with the increase in the incident energy of the positron and vice versa occurred for the irradiated sample, which was in good agreement with the theoretical analysis.

Due to the fact that each kind of annihilation site can be described via one *S*-*W* parameter couple, therefore, it is therefore possible that the type of defects can be reflected by the *S*-*W* curve. Studies have shown that for the same type of defects, the trends of the *S*-*W* curve are consistent [32, 33]. By contrast, the irradiation dose of this experimental process is relatively high, thereby resulting in significant difference in the *S*–*W* curves obtained by irradiated and unirradiated samples. As denoted in Fig. 6, the *S*–*W* curve of the unirradiated sample was linear, indicating that the internal defect type of the material is a single vacancy-type defect (vacancies), and the vacancy was formed during the solution treatment. The *S*–*W* curves of the irradiated samples were much more complicated. Under the two different doses of irradiation, the *S*–*W* curve coincidence degree was higher in the deep range, suggesting similar type of defects in the irradiated samples. However, at higher doses, the *W* parameter of the *S*–*W* curve in the near surface changed greatly. It can be speculated that the number density or size of the defects in the material at high doses is different from samples with low doses of irradiation.

3.2 Radiation-Induced Defects

To verify the results of PAS analysis, TEM characterization on the irradiated samples was performed. It is known that typical irradiation-induced microstructural features in austenitic stainless steel are Frank dislocation loops, network dislocations, cavities and precipitates [25]. The relevant defects are strongly dependent on the irradiation temperature [34]. In the low-temperature regime (below 300 °C), the dominant type of the defects is "black spot", faulted dislocation loops and network dislocations [35]. The results show that the defects caused by Fe ions irradiation in austenitic stainless

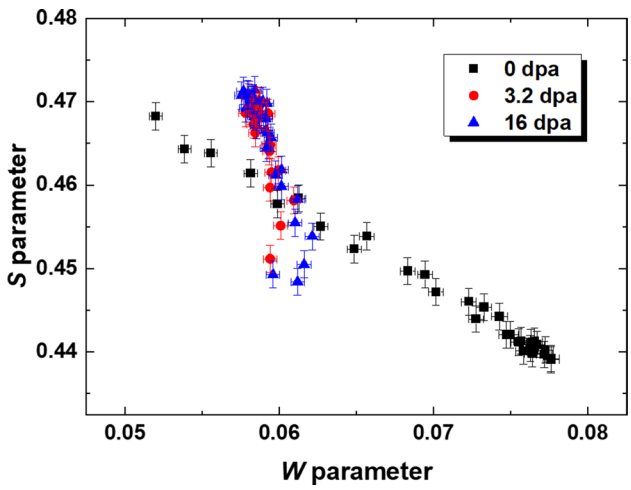

Fig. 6 *S* parameter versus *W* parameter plots for the three kinds of samples

steel were mainly Frank dislocation loops (Fig. 7). The loop size and number density were statistically analyzed, and the results are shown in Fig. 8. The sizes of the dislocation loop at the low doses were relatively uniform with an average size of 16.4 nm. At high doses, the size distribution of the dislocation loop varied a lot. The largest dislocation loop size reached up to 96.3 nm, and the average size was 20.8 nm, which also increased. However, due to the significant recombination under self-ion high damage rate, number density of the loops at high doses was therefore decreased and this was consistent with the results of positron annihilation. Furthermore, it can be suggested that during the long-term irradiation process, along with the recovery of the primary knock-on atoms and vacancies, the dislocation loop can be further evolved into large loops through coalescence of small ones. Thus, the average loop size became larger, while number density reduced, as reported in other studies [36]. In spite of large amount of dislocation loops, no such visible cavities or voids were observed, indicating that the vacancies were either formed in solution or in some form of clusters that are sub-resolvable[37]. This can be expected from the PAS results, as shown in Fig. 4. Additionally, under higher dose irradiation, large dislocations tend to tangle into dislocation network, as shown in Fig. 7d. It has been reported that Frank loops and dislocation network exhibit a rapid evolution at low doses, and then tend to saturate at higher dose. This saturation is due to the dynamic balance between the formation of the Frank loop and its disappearance [38]. Once the faulted loops transform into the upfaulted ones, consequent formation of dislocation network is thus expected. As mentioned before, the Burgers vector of the Frank loop is $\boldsymbol{a}/3\langle 111\rangle$, which is perpendicular to the slip plane $\{111\}$. Along with the formation of dislocation network, the emergence of the sessile character of the Frank loop in the material is the primary cause of the irradiation-induced hardening phenomenon.

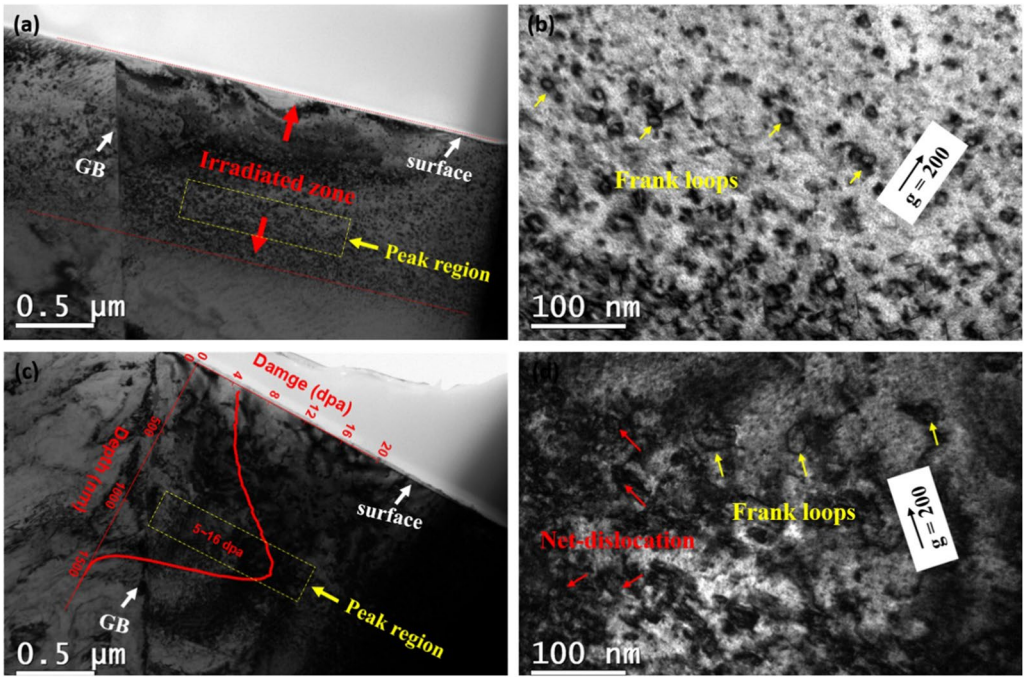

Fig. 7 Morphologies of the cross sections of the irradiated samples: **a** bright-field TEM image of 3.2 dpa sample, **b** morphology of irradiation-induced defects of 3.2 dpa sample, **c** bright-field TEM image of 16 dpa sample, **d** morphology of irradiation-induced defects of 16 dpa sample

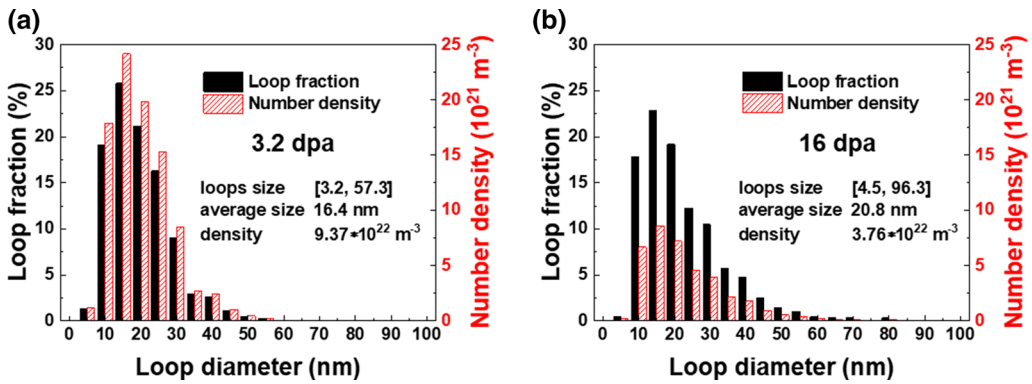

Fig. 8 Comparison of the diameter and number density of Frank loops: **a** 3.2 dpa sample, **b** 16 dpa sample

3.3 Irradiation Hardening

Surface morphology and indentation distribution are shown in Fig. 9. Different morphologies can be seen from SEM photographs. For the unirradiated sample, grain boundary can be easily recognized and the surface of the sample was rather smooth. In contrast, the grain boundary profiles of the irradiated sample were blurred, especially for the high-dose irradiated sample, which has a fuzzy-like surface. This was due to the long-term ion bombardment on the surface. Apart from this, all the indents were uniformly distributed and no inclusions encountered, indicating that all test results were accurate and reliable.

Nanoindentation results are shown in Fig. 10. Affected by the test, results obtained in the near-surface region (~ 50 nm) were abandoned due to the tip fluctuation [39]. It can be seen that with the increase in indentation depth, the hardness value decreased gradually, as noticed in the "indentation size effect" [19]. Figure 10b shows the result of 3.2 dpa sample. The hardness value of the sample increases significantly after irradiation. Furthermore, it was noticed that the hardness value varied greatly in the near-surface region of 200 nm (as shown in Fig. 10b). Furthermore, Fig. 10c shows the hardness result of 16 dpa sample, which also increased significantly. However, the change of the hardness value in the near-surface region of 200 nm was not as obvious as the 3.2 dpa sample. The comparison results of irradiated samples and unirradiated samples are shown in Fig. 10d. In the near-surface 150 nm region, low-dose (3.2 dpa) irradiated sample exhibits the highest hardness value, while after 200 nm, high-dose (16 dpa) irradiated sample topped in values. This coincides with the positron annihilation results. For the high-dose irradiated sample, the evolution process resulted in the decrease in the loop number density and increase in the loop size, which has been confirmed by the TEM observation. When the indentation depth is shallow (less than 150 nm), the corresponding plastic zone and damage level are rather small. In this case, low density Frank loops could not serve as the effective barrier for the dislocation gliding, therefore showing a less hardening behavior. As a result, this phenomenon exists till the indenter tip reaches a critical depth that covers the whole region of the irradiation. It should be noted that the nanoindentation result is a hardness value derived from the contribution of a total of about 5 times the penetration depth of the

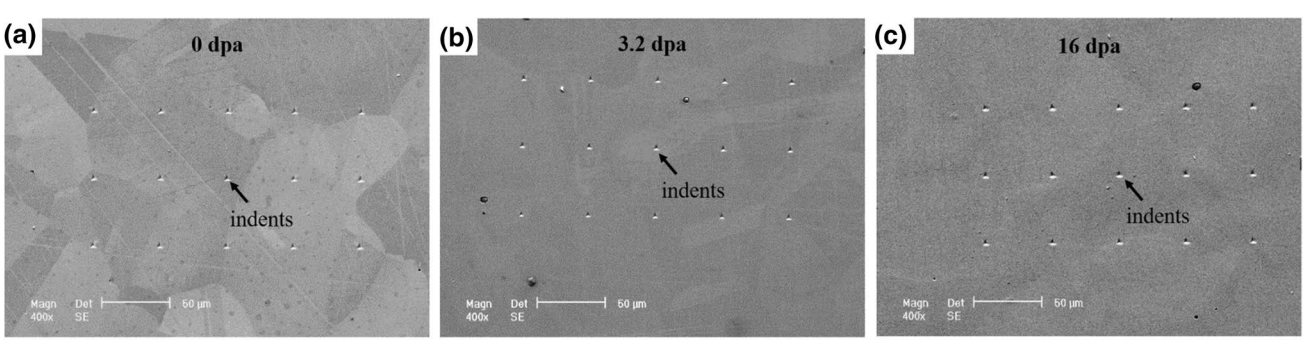

Fig. 9 SEM micrographs of the all samples after indentation tests. Note that surface morphologies were different that grain boundaries were clear for unirradiated sample, while it became obscure for the irradiated samples

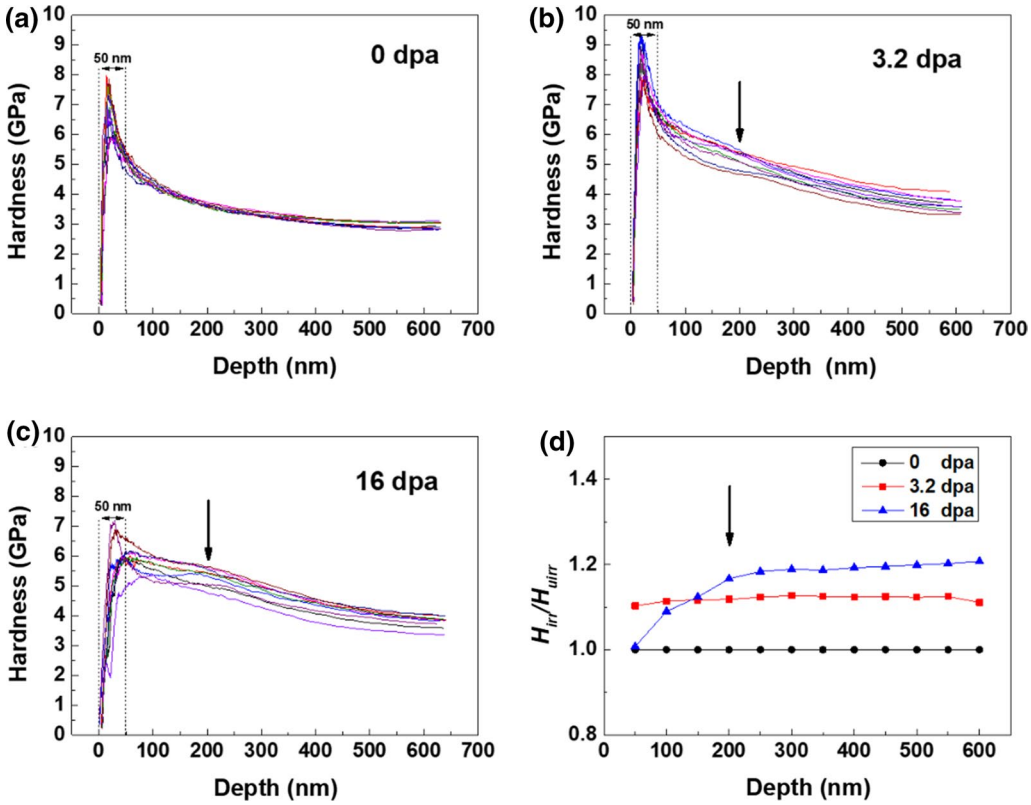

Fig. 10 Dependence of nanohardness of 304SS on the indentation depth of **a** unirradiated sample, **b** irradiated for 3.2 dpa, **c** irradiated for 16 dpa, **d** H_{irr}/H_{unirr} versus depth plot of all samples

indenter [40, 41]. Combined with the SRIM simulation and PAS results, the hardness measurement within the 200 nm range can more accurately reflect the radiation-induced hardening level.

It can be seen from Fig. 10 that the indentation size affects the hardness measured value. To solve this problem, Nix and Gao proposed a model [42], basing on the geometry necessary dislocations:

$$H = H_0\sqrt{1 + h^*/h}, \tag{4}$$

where H is measured value, H_0 is the hardness at the infinite depth of the matrix, h is depth of the indenter, h^* is the critical depth, which is related to the shape of the indenter.

Figure 11 shows that the H^2–$1/h$ curve of the unirradiated sample is approximately linear, indicating the change in the nanohardness measurement is in good agreement with the Nix-Gao model. For the irradiated samples, the H^2–$1/h$ curves of the samples under two doses showed a "bilinear" relationship, similar to what has been reported in previous literature [40, 43]. The H^2–$1/h$ curve has a good linear relationship in the range of 50 to 200 nm near the surface. Beyond this region, the hardness value continues to decrease, from which point the "soft substrate effect" begins

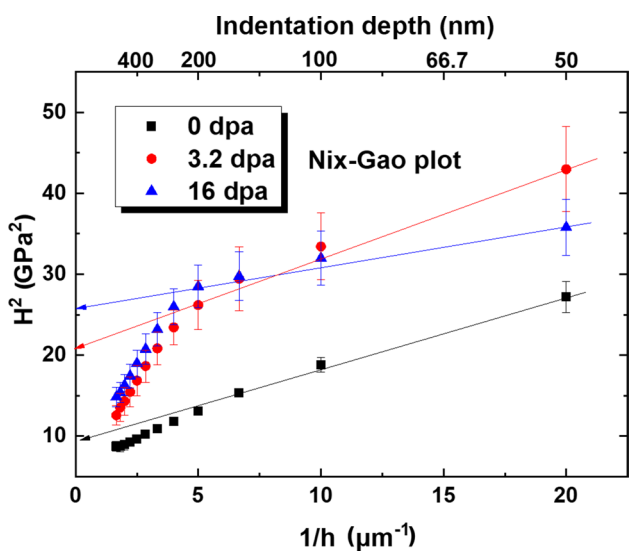

Fig. 11 H^2 versus $1/h$ (indentation depth) plot of the indentation results (Nix-Gao plot)

to increase. Therefore, 200 nm can be regarded as the critical depth. Hardness measurement at the depth of 200 nm can reflect the hardening effect of the entire irradiation damage

Table 2 Nix-Gao model plot results

304SS (dpa)	H_0 (GPa)	h^* (nm)	h_{crit} (nm)	$\Delta H_0/H_0$ (irradiation hardening)
0 dpa	3.01	101.4	200	–
3.2 dpa	4.67	49.3	200	55%
16 dpa	5.16	17.8	200	71%

area. A linear fit was taken of the hardness measurement points in the range of 50 to 200 nm in the H^2–$1/h$ curve, and the results are shown in Table 2.

The hardness of unirradiated 304 SS was 3.01 GPa, while that of the irradiated sample (3.2 dpa) was 4.67 GPa, which increased by 55%. Furthermore, when the irradiation dose increased to 16 dpa, the hardness reached up to 5.16 GPa, which is a 71% increase in hardness value as compared to the unirradiated sample (as shown in Fig. 11). It can be seen that under Fe ions irradiation, the degree of irradiation hardening is prone to be saturated with an increase in irradiation dose from 3.2 to 16 dpa.

The hardness measured by nanoindentation could be converted into Vickers hardness [44]:

$$H_v = 0.0945 H_{\mathrm{Berk}}. \tag{5}$$

Also, Busby et al. [45] proposed an equation to evaluate the yield strength from the increased micro-hardness:

$$\Delta\sigma_y = 3.03 \Delta H_v. \tag{6}$$

From Figs. 10 and 11, we can notice that significant irradiation hardening was observed for the irradiated samples but reaches its peak of saturation at 3.2 dpa dose. Yield strength obtained from Eq. (6) showed an increase trend with increase in dose of irradiation. The variation of yield strength was consistent with the previous results [45, 46].

According to the "Dispersed barrier hardening" (DBH) model proposed by Seeger et al. [47], the microstructural defects like vacancies, interstitial atoms, dislocation loops and other defects caused by irradiation are the root cause of hardening of the material, as they could act as barrier to dislocations movement. Equation (5) gives the increase in hardening caused by irradiation:

$$\Delta\sigma = \alpha \cdot M \cdot G \cdot b \cdot \sqrt{N \cdot d}, \tag{7}$$

where α is the obstacle strength (0.6) varying between 0 and 1, determined by type of the defect, M is the Taylor factor (3.06), G is the shear modulus (76 GPa), b is the value of the Burgers vector (2.5×10^{-8} cm), and N and d are the defect density and the average size, respectively. According to the above formulas, the Vickers hardness, the increment of yield strength of the material and the increment of yield strength obtained from DBH calculation can be calculated, as shown in Table 3. As seen from Table 3, the yield strength of the material at low doses increased to 1367.5 MPa, which was even higher than the calculated yield strength increment (975.6 MPa) at high doses. This was inconsistent with the nanoindentation measurement results. The reason for this result is due to the distribution of irradiation-induced defects, which were not uniform. The defect density is highest at the damage peak (Fig. 7), leading to a higher value obtained from calculation than the actual value obtained from the data (as shown in Table 3). Meanwhile, the actual hardness measurement obtained at 16 dpa dose showed a higher value than that of the calculated value. This indicates that the choice of α in the formula is very important, depending on the size of the irradiation-induced defects. Previous work [48] pointed out that the large-sized Frank dislocation loop was a more effective barrier for the dislocation movement than the small-size loop. The value of α would change as a function of the loop density and size [49]. As discussed before, once the faulted loops transform into the upfaulted ones during irradiation, consequent formation of dislocation network is thus expected (as indicated in Fig. 7d), and this may change the nature of barrier strength. Therefore, when the yield strength is theoretically calculated (Eq. (7)), the value of α (barrier strength) should be employed more carefully.

4 Conclusions

Domestic nuclear 304 stainless steel was irradiated with 3.5 MeV Fe ion at room temperature. Microstructural defects and radiation hardening phenomenon of the material were characterized by PAS, TEM and nanoindentation. The following results are obtained:

1. Irradiation-induced defects were detected by PAS. The discrepancy of the S-W curves of the irradiated samples indicated different characters of the defects.
2. Irradiation-induced Frank loops were observed through TEM characterization. During the long-term irradiation, the Frank loops grew into large-sized loop by the coalescence of small-sized loops, thereby leading to the increase in average loop size and decrease in number density.

Table 3 Comparison of hardness and yield strength of all samples

304SS (dpa)	H_0 (GPa)	ΔH_v(MPa)	$\Delta\sigma_y$(MPa)	$\Delta\sigma'_y$(MPa)
0	3.01	0	0	0
3.2	4.67	156.9	475.3	1367.5
16	5.16	203.2	615.6	975.6

3. Nanoindentation test results showed obvious radiation hardening phenomenon. The level of the hardening increased with increase in irradiation dose. Irradiation-induced Frank loops and the emergence of dislocation network are the root cause of the hardening phenomenon. Statistical analysis suggests the barrier strength of the Frank loop depends on the loop size and number density.

Acknowledgements This work was financially supported by the National Natural Science Foundation (No. 51771211); the National Key Research and Development Program of China (Nos. 2016YFE0105200 and 2017YFB0702100); the Key Research Program of Frontier Sciences, Chinese Academy of Sciences (No. QYZDY-SSWJSC012); the Key Program of the Chinese Academy of Sciences (No. ZDRW-CN-2017-1). The authors would like to thank to all the staff members of 320 kV High-voltage Experimental Platform in Lanzhou and experiment members of Institute of High Energy Physics, Chinese Academy of Sciences in Beijing for their close cooperation and discussion.

References

[1] W.M. Tian, Y.J. Ai, S.M. Li, N. Du, C. Ye, Acta Metall. -Engl. Lett. **28**, 430 (2015)
[2] S.J. Zinkle, G.S. Was, Acta Mater. **61**, 735 (2013)
[3] W.C. Dong, D.B. Gao, S.P. Lu, Acta Metall. -Engl. Lett. **32**, 618 (2018)
[4] M.N. Gussev, E. Cakmak, K.G. Field, J. Nucl. Mater. **504**, 221 (2018)
[5] G.S. Was, S.M. Bruemmer, J. Nucl. Mater. **216**, 326 (1994)
[6] A.B. Du, W. Feng, H.L. Ma, T. Liang, D.Q. Yuan, P. Fan, Q.L. Zhang, C. Huang, Acta Metall. -Engl. Lett. **30**, 1049 (2017)
[7] S.J. Zinkle, Phys. Plasmas **12**, 058101 (2005)
[8] G.S. Was, J.T. Busby, Philos. Mag. **85**, 443 (2006)
[9] P. Scott, J. Nucl. Mater. **211**, 101 (1994)
[10] Z. Jiao, G.S. Was, J. Nucl. Mater. **382**, 203 (2008)
[11] P.L. Andresen, M.M. Morra, J. Nucl. Mater. **383**, 97 (2008)
[12] G.S. Was, Z. Jiao, E. Getto, K. Sun, A.M. Monterrosa, S.A. Maloy, O. Anderoglu, B.H. Sencer, M. Hackett, Scr. Mater. **88**, 33 (2014)
[13] G.S. Was, J. Mater. Res. **30**, 1158 (2015)
[14] R. Kasada, S. Konishi, K. Yabuuchi, S. Nogami, M. Ando, D. Hamaguchi, H. Tanigawa, Fusion Eng. Des. **89**, 1637 (2014)
[15] J. Gupta, J. Hure, B. Tanguy, L. Laffont, M.C. Lafont, E. Andrieu, J. Nucl. Mater. **476**, 82 (2016)
[16] G. S. Was, R. S. Averback, in Comprehensive Nuclear Materials (Elsevier Ltd, 2012), pp. 195.
[17] Z.J. Jiao, G. Was, T. Miura, K. Fukuya, J. Nucl. Mater. **452**, 328 (2014)
[18] C.D. Hardie, S.G. Roberts, A.J. Bushby, J. Nucl. Mater. **462**, 391 (2015)
[19] P. Hosemann, D. Kiener, Y.Q. Wang, S.A. Maloy, J. Nucl. Mater. **425**, 136 (2012)
[20] S. Dannefaer, G.W. Dean, D.P. Kerr, B.G. Hogg, Phys. Rev. B **14**, 2709 (1976)
[21] J.F. Ziegler, M.D. Ziegler, J.P. Biersack, Nucl. Instrum. Methods Phys. Res. Sect. B **268**, 1818 (2010)
[22] R.E. Stoller, M.B. Toloczko, G.S. Was, A.G. Certain, S. Dwaraknath, F.A. Garner, Nucl. Instrum. Methods Phys. Res. Sect. B **310**, 75 (2013)
[23] S.J. Zinkle, L.L. Snead, Scr. Mater. **143**, 154 (2018)
[24] H.P. Zhu, Z.G. Wang, X. Gao, M.H. Cui, B.S. Li, J.R. Sun, C.F. Yao, K.F. Wei, T.L. Shen, L.L. Pang, Y.B. Zhu, Y.F. Li, J. Wang, P. Song, P. Zhang, X.Z. Cao, Nucl. Instrum. Methods Phys. Res. Sect. B **344**, 5 (2015)
[25] C. Pokor, Y. Brechet, P. Dubuisson, J.P. Massoud, A. Barbu, J. Nucl. Mater. **326**, 19 (2004)
[26] W.C. Oliver, G.M. Pharr, J. Mater. Res. **7**, 1564 (2011)
[27] J. Algers, P. Sperr, W. Egger, G. Kögel, F.H.J. Maurer, Phys. Rev. B **67**, 125404 (2003)
[28] A.P. Mills, R.J. Wilson, Phys. Rev. A **26**, 490 (1982)
[29] J. Mäkinen, A. Vehanen, P. Hautojärvi, H. Huomo, J. Lahtinen, R.M. Nieminen, S. Valkealahti, Surf Sci. **175**, 385 (1986)
[30] D.T. Britton, P.C. Riceevans, J.H. Evans, Phil. Mag. Lett. **57**, 165 (1988)
[31] H. Zhu, Z.G. Wang, M.H. Cui, B.S. Li, X. Gao, J.R. Sun, C.F. Yao, K.F. Wei, T.L. Shen, L.L. Pang, Y.B. Zhu, Y.F. Li, J. Wang, E.Q. Xie, Appl. Surf. Sci. **326**, 1 (2015)
[32] Q. Xu, K. Sato, X.Z. Cao, P. Zhang, B.Y. Wang, T. Yoshiie, H. Watanabe, N. Yoshida, Nucl. Instrum. Methods Phys. Res. Sect. B **315**, 146 (2013)
[33] X.B. Liu, R.S. Wang, J. Jiang, Y.C. Wu, C.H. Zhang, A. Ren, C.L. Xu, W.J. Qian, J. Nucl. Mater. **451**, 249 (2014)
[34] P.J. Maziasz, J. Nucl. Mater. **205**, 118 (1993)
[35] D.J. Edwards, E.P. Simonen, S.M. Bruemmer, J. Nucl. Mater. **317**, 13 (2003)
[36] Z.C. Zheng, Y.X. Yu, W.P. Zhang, Z.Y. Shen, F.F. Luo, L.P. Guo, Y.Y. Ren, R. Tang, Acta Metall. -Engl. Lett. **30**, 89 (2016)
[37] B.H. Sencer, G.M. Bond, M.L. Hamilton, F.A. Garner, S.A. Maloy, W.F. Sommer, J. Nucl. Mater. **296**, 112 (2001)
[38] J. Malaplate, B. Michaut, A.R. Laborne, T. Jourdan, F. Dalle, J. Ribis, B. Radiguet, F. Sefta, B. Decamps, J. Nucl. Mater. **517**, 201 (2019)
[39] E.H. Lee, Y. Lee, W.C. Oliver, L.K. Mansur, J. Mater. Res. **8**, 377 (2011)
[40] K. Yabuuchi, Y. Kuribayashi, S. Nogami, R. Kasada, A. Hasegawa, J. Nucl. Mater. **446**, 142 (2014)
[41] C.D. Hardie, S.G. Roberts, J. Nucl. Mater. **433**, 174 (2013)
[42] W.D. Nix, H.J. Gao, J. Mech. Phys. Solids **46**, 411 (1998)
[43] R. Kasada, Y. Takayama, K. Yabuuchi, A. Kimura, Fusion Eng. Des. **86**, 2658 (2011)
[44] A. Lupinacci, K. Chen, Y. Li, M. Kunz, Z. Jiao, G.S. Was, M.D. Abad, A.M. Minor, P. Hosemann, J. Nucl. Mater. **458**, 70 (2015)
[45] J.T. Busby, M.C. Hash, G.S. Was, J. Nucl. Mater. **336**, 267 (2005)
[46] C. Pokor, Y. Brechet, P. Dubuisson, J.P. Massoud, X. Averty, J. Nucl. Mater. **326**, 30 (2004)
[47] A. K. Seeger, Report No. A/CONF.15/P/998, 1959.
[48] A.S. Rao, Nucl. Eng. Des. **269**, 78 (2014)
[49] O. El-Atwani, J.S. Weaver, E. Esquivel, M. Efe, M.R. Chancey, Y.Q. Wang, S.A. Maloy, N. Mara, J. Nucl. Mater. **509**, 276 (2018)